RESEARCH ARTICLE

Check for updates

Bimetal-doped cobalt oxyhydroxides/hydroxides synthesized by electrochemistry for enhanced OER activity†

Rongmei Zhu,*[a] Yi Zhang,[a] Limei Liu,[a] Yong Li,[a] Gaihua He [ID][b] and Huan Pang [ID] *[a]

Metal hydroxides and oxyhydroxides are efficient catalysts for electrochemical oxygen evolution reactions. Herein, we employed a Co-MOF with a tunable structure, high porosity and easy preparation as a precursor to synthesize a bimetal-doped oxyhydroxide/hydroxide electrocatalyst by sequential electrochemical-Lewis acid co-etching and electrosorption doping. This unique co-etching method successfully introduced the high-valent metal ion Hf^{4+}, as well as the electrosorption efficiently doped Fe^{3+}, into the catalyst. Experimental studies and theoretical simulations indicate that the introduction of Hf^{4+} optimized the OER kinetics, and the introduction of Fe^{3+} lowered the overpotential. This synthetic strategy of doping high-valent metal ions provides a new avenue for designing high-performance electrocatalysts.

Introduction

The oxygen evolution reaction (OER) is an important reaction involved in many energy conversion systems such as water splitting and metal–air batteries.[1,2] However, the OER is a four-electron process that results in slow kinetics.[3,4] Therefore, the development of efficient and competitive OER electrocatalysts can effectively improve the cost competitiveness of energy conversion. Among the many OER catalytic materials, noble metal catalysts such as IrO_2 and RuO_2 are often adopted as standards, which exhibit good performance.[5,6] In order to reduce the cost, scientists developed many low-cost, highly active catalysts, such as metal oxide, nitride, phosphide, and sulfide-based catalysts, as well as metal hydroxides and oxyhydroxides.[7–11] Many ways have been explored to improve the charge transfer performance of non-precious metal catalysts, such as morphology modification, interfacial engineering, and the introduction of heteroatoms.[12–16] Among these, the introduction of heteroatoms is capable of modifying the crystal structure and ameliorating the electron transfer of the host material, effectively lowering the energy barriers of reaction intermediates.[17,18] Many recent studies showed that high valence metal ions, such as Fe^{3+}, Cr^{3+}, Ga^{3+}, Zr^{4+}, and W^{4+},[19–24]

can lead to the effective modulation and satisfactory performance of the parent materials in electrocatalysis.

Metal organic frameworks (MOFs), consisting of metal ions or clusters coordinated to organically linked molecules, have been of interest in the field of electrochemical research since the last few decades.[25,26] Due to their structural flexibility and rich porosity, electrocatalysts formed by MOFs as templates usually present rapid diffusion of mass and fast transfer of electrons, therefore resulting in high catalytic activity.[27,28] The most typical example is the conversion of MOF substrates to oxyhydroxides, which are also currently recognized as the true catalytically active species for most OER catalysts.[29,30] For example, Tian *et al.* synthesized a CoFe-MOF and converted it into FeCo-oxyhydroxide with the assistance of electric fields, resulting in high OER activity.[31] The element Hf can be oxidized to stable Hf^{4+}, which is in a high valence state and has the potential to improve the electrocatalytic performance when doped into suitable substrates.[32] However, the atomic radius, electronic structure, and coordination environment of Hf^{4+} are far from those of common transition metal atoms such as Co and Fe. It is somehow difficult to dope Hf^{4+} into hydroxides or oxyhydroxides containing Co and Fe while maintaining the catalyst structure and high accessibility. Therefore, it is crucial to find an excellent precursor to embed Hf for highly active electro-catalysis.

Therefore, in this work, we designed a unique etching procedure followed by electrosorption to fabricate a kind of trimetal oxyhydroxide/hydroxide composite $(Fe,Hf)CoOOH/Co(OH)_2$ based on an easily obtainable Co-MOF. Briefly, the layer structure of the Co-MOF was gradually exfoliated in an alkaline electrolyte containing $HfCl_4$ as a Lewis acid and recombined into a

[a]School of Chemistry and Chemical Engineering, Institute for Innovative Materials and Energy, Yangzhou University, Yangzhou, 225009 Jiangsu, P. R. China. E-mail: rmzhu@yzu.edu.cn, huanpangchem@hotmail.com, panghuan@yzu.edu.cn
[b]School of Pharmaceutical Sciences, Jinzhou Medical University, Jinzhou 121001, P. R. China
†Electronic supplementary information (ESI) available. See DOI: https://doi.org/10.1039/d4qi00823e

layered oxyhydroxide–hydroxide composite $(Hf)CoOOH/Co(OH)_2$ *via* electrochemical activation. Subsequently, Fe^{3+} was doped into the $(Hf)CoOOH/Co(OH)_2$ composite by anodic electrochemical adsorption to form highly active $(Fe,Hf)CoOOH/Co(OH)_2$. The synthetic procedure is shown in Scheme 1 and the resulting $(Fe,Hf)CoOOH/Co(OH)_2$ exhibits distinguishing performance in OER catalysis.

Results and discussion

Scanning electron microscopy (SEM) was used to investigate the morphology of $(Hf)CoOOH/Co(OH)_2$ and $(Fe,Hf)CoOOH/Co(OH)_2$. As shown in Fig. S1,† the Co-MOF is uniformly grown on a carbon paper substrate, and the morphology of the Co-MOF presents as interwoven nanosheets instead of the traditional rhombic dodecahedron or leaf-like shapes. Fig. 1a1, b1, a2 and b2 demonstrate the morphologies of the interwoven nanosheets of $(Hf)CoOOH/Co(OH)_2$ and $(Fe,Hf)CoOOH/Co(OH)_2$ which are inherited from the Co-MOF, respectively. Such morphologies mean that the interactions and connections between the nanosheets are very stable, demonstrating a porous and open structure, which would facilitate the adsorption and diffusion of mass.

To observe the details of the samples more clearly, we used ultrasonic equipment to peel the nanosheets from the carbon paper. The morphology and structure of the $(Hf)CoOOH/Co(OH)_2$ and $(Fe,Hf)CoOOH/Co(OH)_2$ samples were observed by transmission electron microscopy (TEM) and high-resolution transmission electron microscopy (HRTEM). As shown in Fig. 1c1 and c2, $(Hf)CoOOH/Co(OH)_2$ and $(Fe,Hf)CoOOH/Co$

$(OH)_2$ exhibit normal nanoflake structures. The nanosheets are slightly broken because of ultrasonic exfoliation. The HRTEM images demonstrate the lattice properties of the two samples, as shown in Fig. 1d1, e1, d2 and e2. Both $(Hf)CoOOH/Co(OH)_2$ and $(Fe,Hf)CoOOH/Co(OH)_2$ exhibit two main lattice stripes which belong to the (101) planes of CoOOH (PDF: 1731), respectively. The corresponding SAED plots, shown in Fig. 1f1 and f2, exhibit two distinct arrays of CoOOH and $Co(OH)_2$, proving that hydroxides and oxyhydroxides co-exist in the obtained catalysts. In addition, the SAED pattern of $(Hf)CoOOH/Co(OH)_2$ exhibited good diffraction arrays, indicating that the introduction of Hf^{4+} did not affect the crystal structure of the oxyhydroxide and hydroxide. Furthermore, electrochemical adsorption of Fe^{3+} did not trigger significant crystallographic transformation, suggesting that most of the Fe^{3+} is incorporated into the catalyst matrix at the atomic scale. Fig. 1g1 and g2 show that O, Co, Fe and Hf are uniformly distributed in both catalyst matrices. This also illustrates that the electrochemical-Lewis co-acid etching method is effectively capable of stabilizing the anchoring of Hf^{4+} in the oxyhydroxide/hydroxide complexes.

In order to avoid the interference from chlorine gas evolution or Hf^{4+} reduction during the electrochemical-Lewis acid co-etching, the etching potential was set to 0–0.6 V (*vs.* Hg/HgO). The cyclic voltammetry (CV) result of the Co-MOF *via* electrochemical-Lewis acid co-etching in a mixed solution of KOH and $HfCl_4$ is shown in Fig. 2a. Two recognizable redox pair peaks are observed at around 0.25 and 0.2 V, which can be attributed to the redox of Hf and Co, respectively. During the co-etching process, Co ions released from the Co-MOF combine with Hf^{4+} and OH^- in the electrolyte and convert to
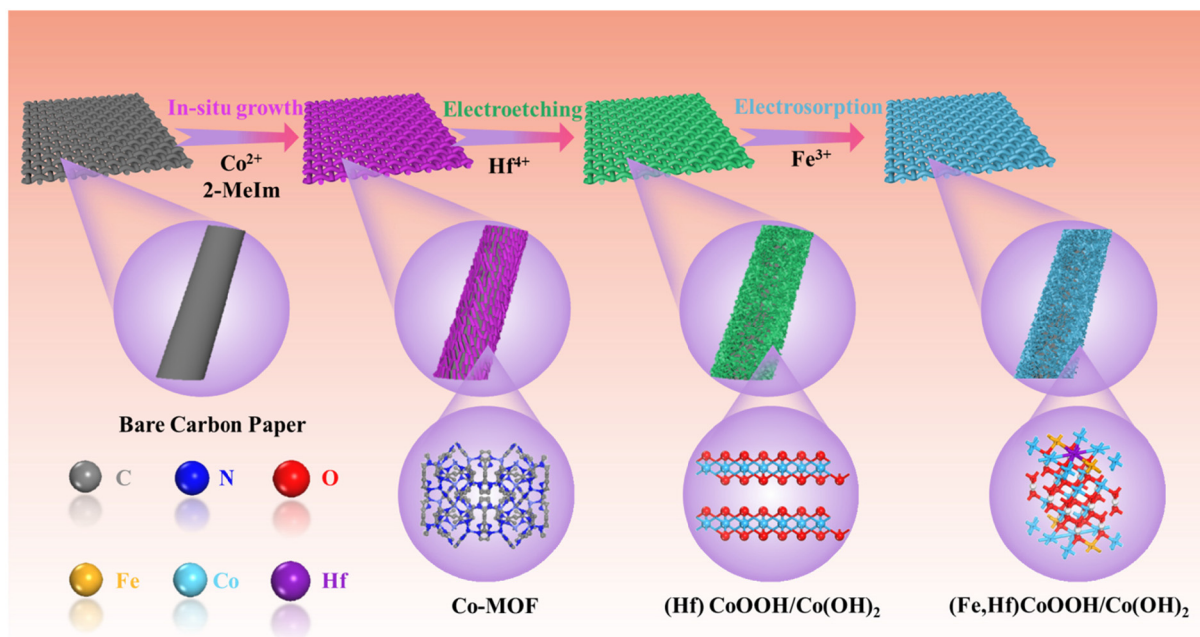
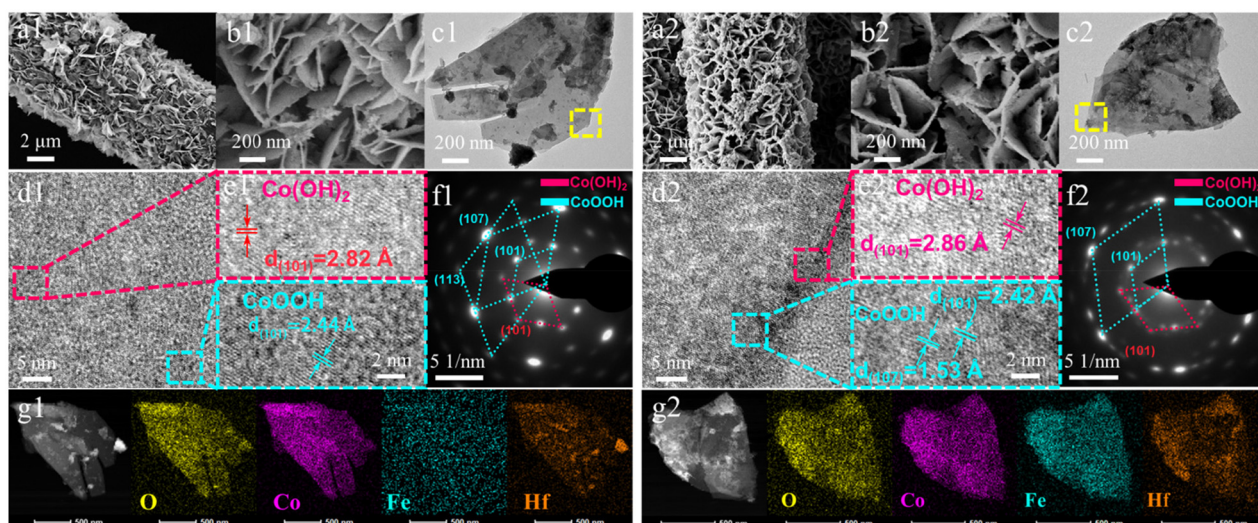**Scheme 1** Schematic illustration of the synthetic process for $(Fe,Hf)CoOOH/Co(OH)_2$.

Fig. 1 Morphological observation and analysis of (Hf)CoOOH/Co(OH)$_2$ and (Fe,Hf)CoOOH/Co(OH)$_2$. SEM images of low magnification of (a1) (Hf)CoOOH/Co(OH)$_2$ and (a2) (Fe,Hf)CoOOH/Co(OH)$_2$ and high magnification of (b1) (Hf)CoOOH/Co(OH)$_2$ and (b2) (Fe,Hf)CoOOH/Co(OH)$_2$. TEM images of (c1) (Hf)CoOOH/Co(OH)$_2$ and (c2) (Fe,Hf)CoOOH/Co(OH)$_2$. HRTEM images and local enlarged images of (d1 and e1) (Hf)CoOOH/Co(OH)$_2$ and (d2 and e2) (Fe,Hf)CoOOH/Co(OH)$_2$. SAED analysis of (f1) (Hf)CoOOH/Co(OH)$_2$ and (f2) (Fe,Hf)CoOOH/Co(OH)$_2$. HAADF-STEM images and the corresponding EDS color mapping of O, Co, Fe, and Hf elements in (g1) (Hf)CoOOH/Co(OH)$_2$ and (g2) (Fe,Hf)CoOOH/Co(OH)$_2$.
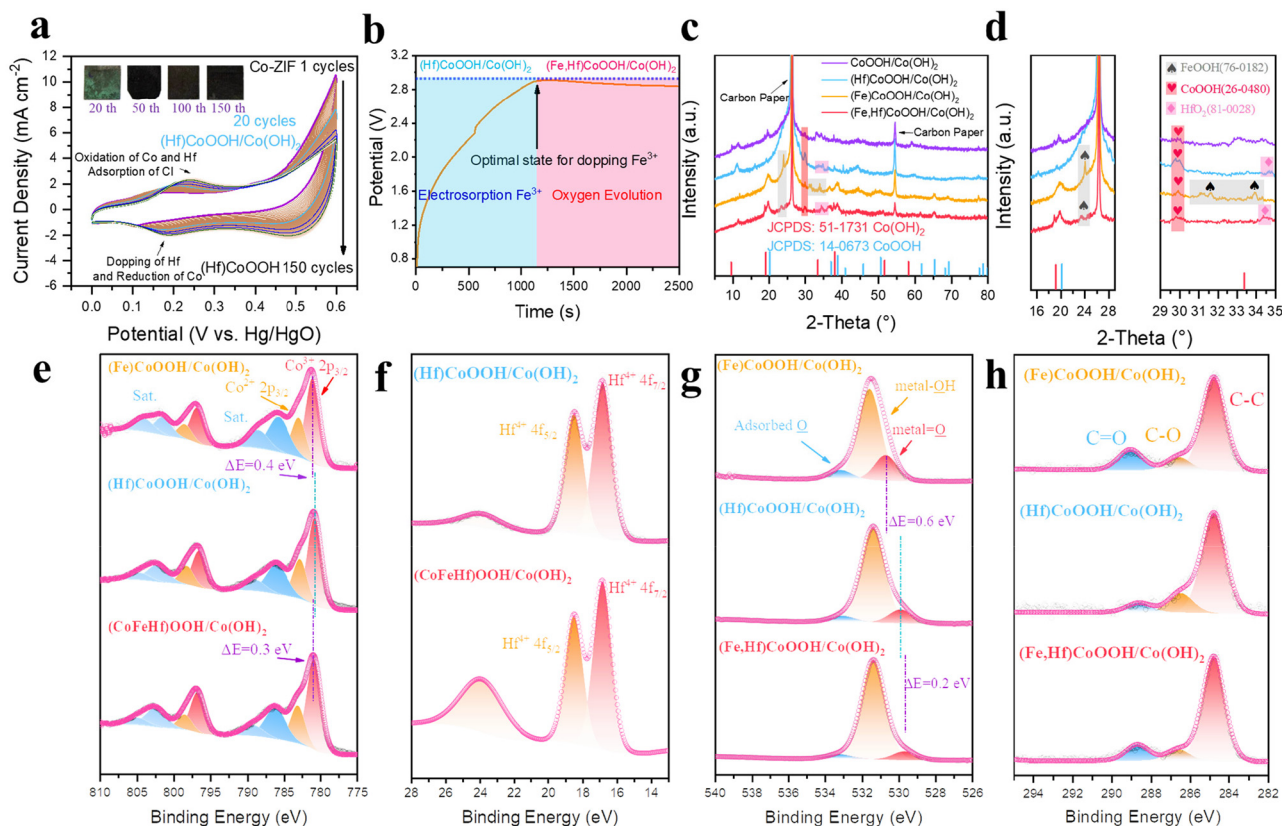

Fig. 2 (a) Electrochemical performance of conversion from the Co-MOF to (Hf)CoOOH/Co(OH)$_2$; inset: optical photos of the Co-MOF undergoing different CV cycles. (b) Galvanostatic electrosorption of Fe towards (Hf)CoOOH/Co(OH)$_2$ for the formation of (Fe,Hf)CoOOH/Co(OH)$_2$. (c) XRD patterns and (d) local enlarged images of CoOOH/Co(OH)$_2$, (Hf)CoOOH/Co(OH)$_2$, (Fe)CoOOH/Co(OH)$_2$, and (Fe,Hf)CoOOH/Co(OH)$_2$. High-resolution XPS spectra of (e) Co 2p (f) Hf 4f, (g) O 2p and (h) C 1s in the samples of (Hf)CoOOH/Co(OH)$_2$, (Fe)CoOOH/Co(OH)$_2$, and (Fe,Hf)CoOOH/Co(OH).

hydroxide and subsequently to oxyhydroxide. Furthermore, chloride ions released from $HfCl_4$ can form ion pairs with Co ions and stabilize the orthotetrahedral coordination structure of $Co(OH)_2$, which facilitates the formation of α-$Co(OH)_2$.[33] Under cathodic current conditions, Hf^{4+} can diffuse toward the working electrode, adsorbing on the $CoOOH/Co(OH)_2$ surface, integrating into the matrix or replacing part of the Co atoms, finally forming $(Hf)CoOOH/Co(OH)_2$.

When the co-etching is completed, almost all Co-MOFs are converted to $(Hf)CoOOH/Co(OH)_2$. However, excessive etching will destroy the coordination structure of $(Hf)CoOOH/Co(OH)_2$, forming β-$Co(OH)_2$ with lower electrochemical activity. In addition, excessive electrochemical Lewis acid co-etching leads to the disruption of the interwoven layered nanostructures and hinders the accessibility of the active sites. As shown in the inset of Fig. 2a, the sample subjected to deep etching also exhibits a color change. Therefore, based on the above analysis, we selected the sample after 20 cycles of etching as the precursor for the subsequent reactions. The precursors were washed with deionized water to remove Cl ions to prevent undesired chlorine gas evolution reactions at high potentials. Furthermore, as shown in Fig. 2b, there exists an optimal electrosorption state at 1150 s when doping Fe into the $(Hf)CoOOH/Co(OH)_2$ catalyst. The maximum voltage limit of 4 V was not reached in the "optimal electrosorption state"; therefore, the voltage drop after this moment is triggered by oxygen evolution instead of discharge. After that moment, $(Fe, Hf)CoOOH$ begins the oxygen evolution reaction, which is reflected by the gradual decrease in the potential required to maintain a constant current.

To investigate the effect of etching time on the conversion of the Co-MOF, we recorded SEM images at different cycle numbers. As shown in Fig. S2a,† it can be concluded that the Co-MOF slightly dissolved after the 5th cycle and the interwoven nanosheets gradually dissolved. After the 10th cycle, the structure of the Co-MOF further broke; notably, some Co-MOFs were exfoliated by etching and the layered structures began to emerge (Fig. S2b†). When the 20th cycle of CV was completed, Co-MOFs almost converted into layered nanostructures, with some lamellar materials arranged disorderly, intertwined and interpenetrated, but without forming the conventional nanoflower (Fig. S2c†). If the cycle exceeds 50 cycles, the excessively co-etched sample is almost dissolved and only a small amount of flake structure remains and the layered structure almost disappears drastically (Fig. S2d–f†).

In order to investigate the effect of doping Hf^{4+} on the crystal structure of oxyhydroxide/hydroxide composites, we prepared Hf-free samples $CoOOH/Co(OH)_2$ and $(Fe)CoOOH/Co(OH)_2$ according to the above electrochemical procedure and analyzed them by the X-ray diffraction (XRD) technique. At first, comparison of the XRD patterns of the four catalysts and Co-MOF (Fig. S3a†) reveals that the Co-MOF precursors are fully converted to the oxyhydroxide/hydroxide composites. In Fig. 2c, the XRD patterns of $CoOOH/Co(OH)_2$, $(Hf)CoOOH/Co(OH)_2$, $(Fe)CoOOH/Co(OH)_2$, and $(Fe,Hf)CoOOH/Co(OH)_2$ are compared. The sharp peaks at 25.1 and 43.5° indicate the

carbon paper substrate. There are three peaks at 19.1, 33.4, and 38.1°, corresponding to the planes of $Co(OH)_2$, and three peaks at 20.1, 36.9 and 38.9° correspond to the planes of CoOOH.

In particular, the XRD pattern of the carbon paper after the electrochemical process is almost the same as that of the bare carbon paper (Fig. S3b†), indicating that the carbon paper can be used as an effective substrate for electrocatalysts. In addition, a minor amount of other compounds is formed during the electrochemical conversion of the Co-MOF to oxyhydroxide/hydroxide. A small amount of FeOOH (JCPDS: 76-0182) was generated during the electrosorption, while $(Hf)CoOOH/Co(OH)_2$ and $(Hf,Fe)CoOOH/Co(OH)_2$ exhibit trace amounts of HfO_2 (JCPDS: 81-0028). Also, a small amount of α-CoOOH (26-0480) was detected in all samples of catalyst. A comparison of the XRD patterns of the four catalysts and Co-MOF (Fig. S3†) reveals that the Co-MOF precursors are fully converted to the oxyhydroxide/hydroxide composites.

Fourier transform infrared (FT-IR) spectra of different catalysts were recorded to analyze the surface functional groups (Fig. S4†). The peaks at 1483 and 519 cm^{-1} are assigned to the metal=O double bond in oxyhydroxide and metal–O stretching vibration, respectively. For the hydroxide, the peak at 635 cm^{-1} can be assigned to the metal–OH stretching vibration. In addition, the peaks located at 1600 and 1376 cm^{-1} are assigned to OH bending in H_2O molecules and CO_3^{2-}, respectively.[34] Notably, the two samples of $(Fe)CoOOH/Co(OH)_2$ and $(Fe,Hf)CoOOH/Co(OH)_2$ that undergo electrosorption of Fe^{3+} exhibit strong metal–O peaks. This is due to the generation of defects and changes in layer spacing, which also promote the electrocatalytic activity. In addition, the metal–N peaks were absent in all four catalysts, which also indicates that the Co-MOF is fully converted into the target catalyst.

In order to investigate the effect of the introduction of Hf^{4+} and Fe^{3+} on the electronic states of the materials, we analyzed $(Fe)CoOOH/Co(OH)_2$, $(Hf)CoOOH/Co(OH)_2$ and $(Fe,Hf)CoOOH/Co(OH)_2$ using X-ray photoelectron spectroscopy (XPS). Fig. S5† reveals the full XPS survey, clearly showing typical peaks at binding energies of 18, 198, 286, 531, 716 and 780 eV, corresponding to the elements Hf, Cl, C, O, Fe, and Co, respectively. The high-resolution XPS for Co $2p_{3/2}$ in $(Fe)CoOOH/Co(OH)_2$ is shown in Fig. 2e. The peaks located at 783.0 and 781.2 eV represent Co_2^+ and Co^{3+} respectively. Due to the specific electro-etching process, the amount of Co^{3+} in both materials is much higher than that of Co_2^+. The high-resolution XPS spectra of Hf in $(Hf)CoOOH/Co(OH)_2$ and $(Fe,Hf)CoOOH/Co(OH)_2$ samples suggested the presence of Hf^{4+}. As can be seen in Fig. 2f, two associated peaks of Hf are located at 16.84 and 18.51 eV, which are classified as $4f_{7/2}$ and $4f_{5/2}$, respectively.[35] As shown in Fig. 2g, the high-resolution XPS spectra of O show three peaks attributed to metal=O, metal–OH, and adsorbed oxygen in oxygen vacancies in all the three samples. In comparison with the other two samples, the apparent downward binding energy shift of the O atom is observed due to the introduction of Hf^{4+}, and similarly, the

5452 | *Inorg. Chem. Front.*, 2024, **11**, 5449–5457

This journal is © the Partner Organisations 2024

binding energy shift of Co is also demonstrated in Fig. 2e. The XPS results demonstrate the electronically tuned formation of (Fe,Hf)CoOOH/Co(OH)$_2$ with an optimal electronic structure for the OER electrocatalysis.[36] The XPS high-resolution spectra of C demonstrate three chemical environments, C–C at 284.8 eV, C–O at 288.7 eV, and C=O at 286.2 eV, in all the above three samples (Fig. 2h). The peak of the C–C bond may originate from the free ligand and the carbon paper substrate. Fig. S6† shows the XPS high-resolution spectra of Fe, which demonstrate the successful doping of the Fe element into (Fe)CoOOH/Co(OH)$_2$ and (Fe,Hf)CoOOH/Co(OH)$_2$ due to electrosorption.

The OER electrocatalytic activity of (Fe,Hf)CoOOH/Co(OH)$_2$ catalysts was tested using a standard three-electrode cell system in 1.0 mol L^{-1} KOH solution at room temperature. In order to demonstrate the importance of Hf^{4+} in the catalysts, we comparatively tested CoOOH/Co(OH)$_2$, (Hf)CoOOH/Co(OH)$_2$, and (Fe)CoOOH/Co(OH)$_2$. The LSV measurement used to test the OER activity is shown in Fig. 3a The overpotentials (η_{10}) of the above four catalysts in descending order are (Fe)CoOOH/Co(OH)$_2$ (203 mV) < (Fe,Hf)CoOOH/Co(OH)$_2$ (250 mV) < CoOOH/Co(OH)$_2$ (295 mV) < (Hf)CoOOH/Co(OH)$_2$ (337 mV). As a result, the introduction of Fe^{3+} is able to greatly reduce the overpotential during the OER process. Even though the overpotential of (Fe,Hf)CoOOH/Co(OH)$_2$ is higher than that of (Fe)CoOOH/Co(OH)$_2$, (Fe,Hf)CoOOH/Co(OH)$_2$ possesses higher activity at potentials beyond 1.51 V (marked as a pink dashed line), with an overpotential of 379 mV for a current density up to 100 mA cm^{-2}. Similarly, the comparison of

CoOOH/Co(OH)$_2$ and (Hf)CoOOH/Co(OH)$_2$ also shows the same result. Therefore, the Hf-doped catalysts show a delayed increase in current density, and Hf^{4+} is able to significantly improve the kinetics during the OER process. Fig. 3b shows that the Tafel slopes of all the samples and that of (Fe,Hf)CoOOH/Co(OH)$_2$ are greatly reduced by the modulation of Hf^{4+}. In addition, the Tafel slope plot at a high potential shows a similar result (Fig. S7†), suggesting that the Hf-doped material possesses excellent electrochemical activity. Notably, the OER catalytic activity of (Hf,Fe)CoOOH/Co(OH)$_2$ also exceeds those of many previously reported Co or Fe-based electrocatalysts under similar conditions as presented in Table S1.†

In order to investigate the effect of the content of Hf^{4+} on the catalytic activity, we explored the OER activity of the catalysts with different doping amounts of Hf^{4+}. (Hf)CoOOH/Co(OH)$_2$-0.75, (Hf)CoOOH/Co(OH)$_2$-1.5 (the abovementioned sample (CoHf)OOH/Co(OH)$_2$), and (Hf)CoOOH/Co(OH)$_2$-2.25 were obtained via etching under identical electrochemical cycles with different HfCl$_4$ concentrations of 0.75 mmol L^{-1}, 1.5 mmol L^{-1}, and 2.25 mmol L^{-1}, respectively. Hf^{4+} and Cl$^-$ modulate the coordination environment of CoOOH/Co(OH)$_2$, and excessive Lewis acid (HfCl$_4$) has a great influence on the conversion of the Co-MOF. As shown in Fig. S8,† the electrolyte with excessive HfCl$_4$ dosage leads to almost complete dissolution of the Co-MOF, instead of being converted to hydroxide. Afterwards, we doped Fe into different Hf-doped samples to obtain the corresponding (Fe,Hf)CoOOH/Co(OH)$_2$-x and examined their OER performance. As shown in Fig. S9,† the
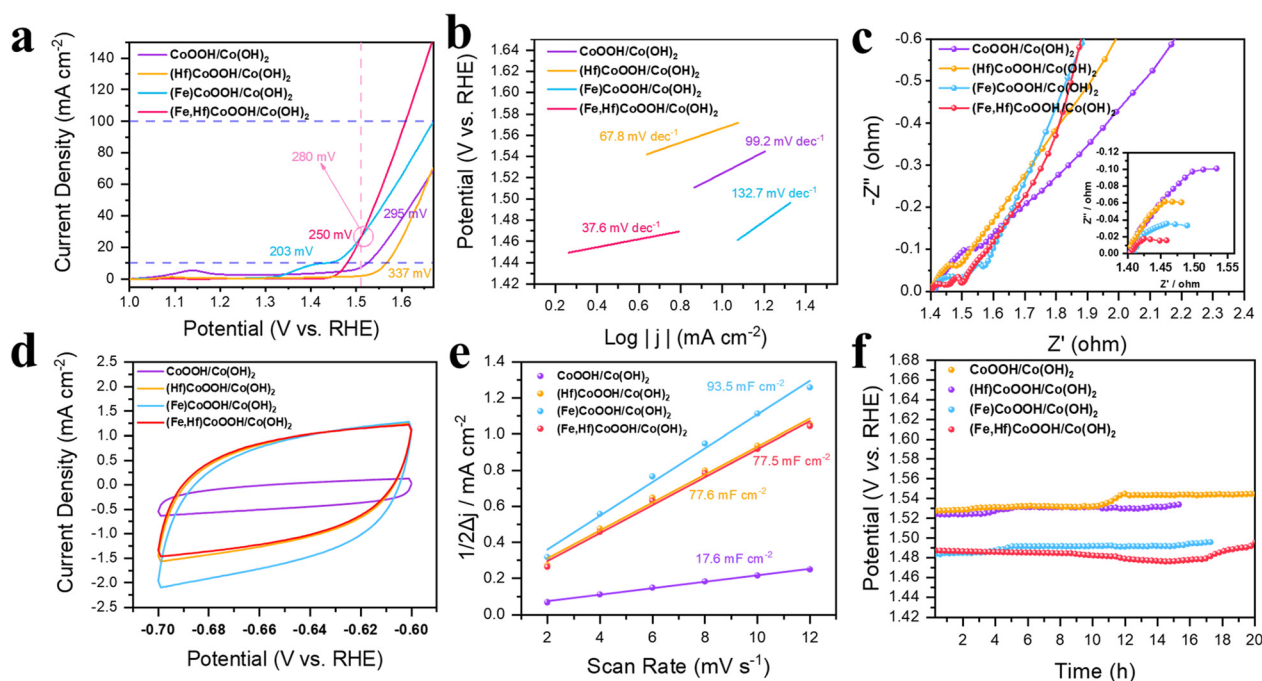

Fig. 3 Electrocatalytic characterization of the synthesized materials toward the OER in 1 M KOH. (a) LSV polarization curves and (b) the corresponding Tafel slopes, (c) EIS analysis, (d) CV measurements at 12 mV s^{-1} sweep rate and (e) the corresponding C_{dl} fitting plots, and (f) stability tests of CoOOH/Co(OH)$_2$, (Hf)CoOOH/Co(OH)$_2$, (Fe)CoOOH/Co(OH)$_2$, and (Fe,Hf)CoOOH/Co(OH)$_2$.

This journal is © the Partner Organisations 2024

Inorg. Chem. Front., 2024, **11**, 5449–5457 | **5453**

electrochemical properties of the obtained samples are different due to the various Hf^{4+} dosages in the samples. A higher content of Hf^{4+} doping (2.25 mmol L^{-1}) would decrease the OER activity of the catalyst. Therefore, optimal Hf^{4+} dosage can significantly improve the OER catalytic activity.

The charge transfer impedance (R_{ct}) can reflect OER kinetics. As can be seen in Fig. 3c from the Nyquist plots, they all possess low and similar impedance values, in which the charge transfer impedance of (Fe)CoOOH/Co(OH)$_2$ and (Fe,Hf) CoOOH/Co(OH)$_2$ is less than 0.15 Ω. This is because the embedding of ions in the Co(OH)$_2$ interlayers improves the electrical conductivity and accelerates the charge transfer rates. Considering that the electrochemically active surface area (ECSA) is positively correlated with the double layer capacitance (C_{dl}), we calculated C_{dl} and ECSA for all four electrocatalysts by collecting the CV distributions in the non-Faraday region. Fig. 3d shows the CV profiles of all four catalysts at 12 mV s^{-1} sweep rate, and Fig. 3e illustrates the fitted C_{dl} values, which illustrates that the doping of Hf^{4+} and Fe^{3+} increased the C_{dl} values of the catalysts. All four catalysts exhibit high C_{dl} values, which suggests that the laminar structure provides sufficient active sites for the catalytic reaction. The CV curves of CoOOH/Co(OH)$_2$, (Hf)CoOOH/Co(OH)$_2$, (Fe) CoOOH/Co(OH)$_2$, and (Fe,Hf)CoOOH/Co(OH)$_2$, which were measured at different scan rates of 2–12 mV s^{-1} in the voltage range −0.7 to −0.6 V *versus* RHE, are displayed in Fig. S10.† Furthermore, the LSV and Tafel slope information normalized by ECSA is shown in Fig. S11,† which demonstrates better OER kinetics of (Fe,Hf)CoOOH/Co(OH)$_2$. Long-term durability is another important parameter for evaluating OER catalysts; therefore, the activities of the catalysts were evaluated by performing continuous OERs in 1 mol L^{-1} KOH electrolyte at a constant current. As shown in Fig. 3f, all the four catalysts exhibited high stability, and no obvious potential fluctuations were found during the 15 h of continuous OERs, which indicates that the catalytic activity of oxyhydroxide/hydroxide composites is not significantly affected by phase transformation.

In order to further explore the effect of the doping of Hf^{4+} and Fe^{3+} on the catalytic activity of (Fe,Hf)CoOOH/Co(OH)$_2$, density-functional theory (DFT) calculations were carried out based on the established crystal models. The model was built by geometry optimization of the 2 × 2 × 1 CoOOH supercell

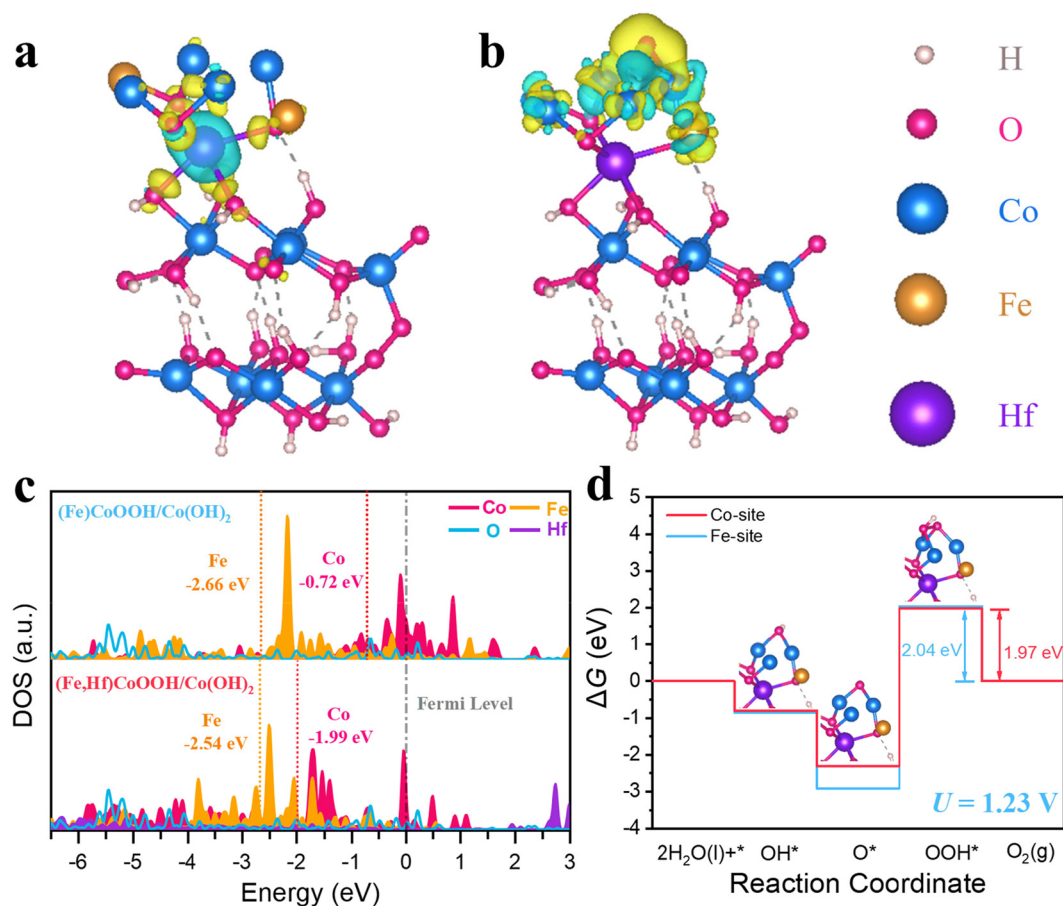**Fig. 4** DFT theoretical calculations and analysis results. Differential charge densities of (a) (Fe,Hf)CoOOH/Co(OH)$_2$ doped with Hf^{4+} and (b) (Fe,Hf) CoOOH/Co(OH)$_2$ doped with O*; yellow and cyan areas represent the electron accumulation and depletion, respectively. (c) The partial density of state (PDOS) plots of potential catalytic sites in (Fe)CoOOH/Co(OH)$_2$ and (Fe,Hf)CoOOH/Co(OH)$_2$. (d) Gibbs free energy diagrams for (Fe,Hf) CoOOH/Co(OH)$_2$ at U = 1.23 V.

5454 | *Inorg. Chem. Front.*, 2024, **11**, 5449–5457

This journal is © the Partner Organisations 2024

(JCPDS 14-0673). As shown in Fig. 4a, the charge density difference plots of (Fe,Hf)CoOOH indicate that the introduction of Hf^{4+} results in a redistribution of the local charge density. In this result, Fe and Co sites show local electron accumulation, while Hf exhibits local electron depletion. Fig. 4b and Fig. S12† illustrate the electronic states between (Fe,Hf)CoOOH/Co(OH)$_2$ and (Fe)CoOOH/Co(OH)$_2$ with O* intermediates. It is obvious that the transfer of electrons from Co atoms to O* takes place, which benefits the evolution of oxygen-containing species. In addition, the partial density of states (PDOS) of (Fe)CoOOH/Co(OH)$_2$ and (Fe,Hf)CoOOH/Co(OH)$_2$ are presented in Fig. 4c. The high overlap of the Co 3d and Fe 3d orbitals with the O 2p orbitals suggests that both (Fe)CoOOH/Co(OH)$_2$ and (Fe,Hf)CoOOH/Co(OH)$_2$ possess strong adsorption of O species. Indeed, the center of the d-band of the active sites decreased from −2.13 to −2.81 eV (Fig. S13†) significantly after the introduction of Hf^{4+}. The incorporation of Hf^{4+} resulting in a downward shift of the metal d-band center could appropriately weaken the strong affinity of the catalyst for OOH*, effectively balancing the adsorption energies of the key intermediates and thus promoting fast OER kinetics of (Fe,Hf)CoOOH/Co(OH)$_2$. Furthermore, as shown in Fig. S14,† the projected density of states of (Fe)CoOOH/Co(OH)$_2$ and (Fe,Hf)CoOOH/Co(OH)$_2$ demonstrate that the introduction of Hf^{4+} changed the electronic state. This change results in enhanced spin polarizability of (Fe,Hf)CoOOH/Co(OH)$_2$ (Fig. S15†), which may enhance the catalytic activity.

When $U = 1.23$ V, as shown in Fig. 4d, the first step (*OH adsorption) of the OER is a spontaneous process at the Co and Fe sites in (Fe,Hf)CoOOH/Co(OH)$_2$.[37] The formation step of *OOH exhibits a high ΔG value, indicating that this is the rate-determining step of the OER. For the O$_2$ release step, the ΔG of (Fe,Hf)CoOOH/Co(OH)$_2$ is lower than that of (Fe)CoOOH/Co(OH)$_2$ (Fig. S16†), suggesting that OOH * species are activated by Hf^{4+}, verifying that the incorporating of Hf^{4+} indeed expedites the reaction kinetics of the OER.

Conclusions

In conclusion, we have successfully synthesized a high-valent Hf^{4+}-doped OER catalyst (Fe,Hf)CoOOH/Co(OH)$_2$ by Lewis acid-assisted electrochemical etching, and the prepared catalyst exhibits efficient and stable performance. The overpotentials of the OER at η_{10} and η_{100} are only 250 and 376 mV, respectively, and can remain stable for a continuous reaction of 20 h. DFT calculations showed that the addition of Hf^{4+} effectively modulates the electronic structure, enhances the adsorption of Co on the intermediates and the release of oxygen, promotes the electrochemical kinetics, and reduces the free energy change in the potential-determining step of the OER. This greatly improves the electrocatalytic activity of the OER. This work emphasizes the role of high-valent Hf^{4+} doping in improving the intrinsic catalytic activity, and this facile doping strategy brings new inspirations for the development of OER catalysts.

Experimental

Pre-treatment of carbon paper

The native carbon paper was placed in a furnace and calcined at 500 °C for 4 h under an ambient atmosphere.

Synthesis of the Co-MOF

1 mmol (0.291 g) of cobalt nitrate hexahydrate was dissolved in 25 mL of deionized water and denoted as solution A. 2.5 mmol (0.2052 g) of 2-methylimidazole were dissolved in 25 mL of deionized water and denoted as solution B. The carbon paper was immersed in solution A and stirred for 2 h. Then solution B was poured into solution A, and then the mixed solution and carbon paper were transferred to the liner of the PTFE reactor. The reactor was sealed and placed in an oven at 160 °C for 8 h. The carbon paper was washed with methanol after the reaction. Finally, the Co-MOF-loaded carbon paper was dried in an oven at 60 °C overnight.

Synthesis of (Hf)CoOOH/Co(OH)$_2$

A certain amount of HfCl$_4$ was added to a solution of 0.1 M KOH. Then the carbon paper loaded with the Co-MOF was placed in the mixed solution. Electrochemical cyclic voltammetry was used for etching under these conditions. The voltage range was set to 0–0.6 V (vs. Hg/HgO) with a sweep rate of 10 mV s^{-1}. Then, the carbon paper was collected after a certain number of cycles until the Co-MOF gradually transformed into green, and it was washed with deionized water.

Synthesis of (Fe,Hf)CoOOH/Co(OH)$_2$

Carbon paper loaded with (Hf)CoOOH/Co(OH)$_2$ was placed in an aqueous solution of 0.15 M ammonium iron sulfate. Fe^{3+} was electrosorbed for 1150 s at a current density of 1 mA cm^{-2} using chronopotentiometry. The high potential limit of chronopotentiometry was set to an unreachable value, which was 4 V in this experiment.

Synthesis of CoOOH/Co(OH)$_2$

The synthesis procedure is consistent with that of (Hf)CoOOH/Co(OH)$_2$, but HfCl$_4$ was not added to the KOH solution.

Synthesis of (Fe)CoOOH/Co(OH)$_2$

The synthesis procedure is the same as that of (Hf)CoOOH/Co(OH)$_2$, but HfCl$_4$ was not added to the KOH solution. The process of electrosorption of Fe^{3+} is consistent with the conversion of (Hf)CoOOH/Co(OH)$_2$ to (Fe,Hf)CoOOH/Co(OH)$_2$ except for the use of carbon paper loaded with CoOOH/Co(OH)$_2$.

Author contributions

Rongmei Zhu conceived the ideas of the experiment. Rongmei Zhu and Yi Zhang wrote the paper. Yi Zhang synthesized the materials and performed the measurements. Limei Liu and Gaihua He helped in testing the electrochemical performance of the material. Yi Zhang and Yong Li were responsible for

Data availability

The data supporting this article have been included as part of the ESI.†

Conflicts of interest

There are no conflicts to declare.

Acknowledgements

References

1 Q. Wang, S. Kaushik, X. Xiao and Q. Xu, Sustainable zinc–air battery chemistry: advances, challenges and prospects, *Chem. Soc. Rev.*, 2023, **52**, 6139–6190.

2 C. Shang, X. Xiao and Q. Xu, Coordination chemistry in modulating electronic structures of perovskite-type oxide nanocrystals for oxygen evolution catalysis, *Coord. Chem. Rev.*, 2023, **485**, 215109.

3 C. Zhao, L. Tian, Z. Zou, Z. Chen, H. Tang, Q. Liu, Z. Lin and X. Yang, Revealing and accelerating interfacial charge carrier dynamics in Z-scheme heterojunctions for highly efficient photocatalytic oxygen evolution, *Appl. Catal., B*, 2020, **268**, 118445.

4 Y. Zhang, X. Zhang, L. Jiao, Z. Meng and H. Jiang, Conductive Covalent Organic Frameworks of Polymetallophthalocyanines as a Tunable Platform for Electrocatalysis, *J. Am. Chem. Soc.*, 2023, **145**, 24230–24239.

5 S. Liu, Y. Zhang, X. Mao, L. Li, Y. Zhang, L. Li, Y. Pan, X. Li, L. Wang, Q. Shao, Y. Xu and X. Huang, Ultrathin perovskite derived Ir-based nanosheets for high-performance electrocatalytic water splitting, *Energy Environ. Sci.*, 2022, **15**, 1672–1681.

6 H. Gao, Z. Xiao, S. Du, T. Liu, Y. Huang, J. Shi, Y. Zhu, G. Huang, B. Zhou, Y. He, C. Dong, Y. Li, R. Chen and S. Wang, Reducing the Ir–O coordination number in anodic catalysts based on IrOx nanoparticles towards

enhanced proton–exchange–membrane water electrolysis, *Angew. Chem., Int. Ed.*, 2023, **62**, e202313954.

7 J. Li, Y. Liu, X. Tang, L. Xu, L. Min, Y. Xue, X. Hu and Z. Yang, Multiwalled carbon nanotubes coated with cobalt (II) sulfide nanoparticles for electrochemical sensing of glucose via direct electron transfer to glucose oxidase, *Microchim. Acta*, 2020, **187**, 80.

8 K. Zhang and R. Zou, Advanced transition metal–based OER electrocatalysts: current status, opportunities, and challenges, *Small*, 2021, **17**, 2100129.

9 R. Gao, J. Zhu and D. Yan, Transition metal-based layered double hydroxides for photo(electro)chemical water splitting: a mini review, *Nanoscale*, 2021, **13**, 13593–13603.

10 T. Zhou, Y. Yang, Y. Jing, Y. Hu, F. Yang, W. Sun and L. He, Defective blue titanium oxide induces high valence of NiFe-(oxy)hydroxides over heterogeneous interfaces towards high OER catalytic activity, *Chem. Sci.*, 2023, **14**, 13453–13462.

11 C. Zheng, B. Huang, X. Liu, H. Wang and L. Guan, Mn-doped RuO_2 nanocrystals with abundant oxygen vacancies for enhanced oxygen evolution in acidic media, *Inorg. Chem. Front.*, 2024, **11**, 1912–1922.

12 F. Li, Y. Li, L. Li, W. Luo, Z. Lu, X. Zhang and Z. Zheng, Heterostructured FeNi hydroxide for effective electrocatalytic oxygen evolution, *Chem. Sci.*, 2022, **13**, 9256–9264.

13 H. Li, H. Liu, F. Wang, G. Li, X. Wang and Z. Tang, Hot electron assisted photoelectrochemical water splitting from Au-decorated $ZnO@TiO_2$ nanorods array, *Nano Res.*, 2022, **15**, 5824–5830.

14 J. Liu, W. Du, S. Guo, J. Pan, J. Hu and X. Xu, Iron–Locked Hydr(oxy)oxide Catalysts via ion–compensatory reconstruction boost large–current–density water oxidation, *Adv. Sci.*, 2023, **10**, 2300717; H. Wang, Y. Liang, S. Liu, X. Mu, H. Yu, K. Deng, Z. Wang, Y. Xu and L. Wang, Electronic and active site engineering in Rh metallene via phosphorus and sulfur dual-doping for electrocatalytic sulfion recycling and hydrogen generation, *Inorg. Chem. Front.*, 2023, **10**, 5686–5693.

15 P. Li, Y. Liu, M. A. Mushtaq and D. Yan, Recent progress in ammonia synthesis based on photoelectrocatalysis, *Inorg. Chem. Front.*, 2023, **10**, 4650–4667.

16 Y. Li, N. Zhu, Z. Su, X. Hu, Z. Dou and Z. Su, An hourglass-shaped nickel-based polyoxometalate crystalline material as a highly efficient bifunctional electrocatalyst for the oxygen evolution reaction and detection of H_2O_2, *Inorg. Chem. Front.*, 2024, **11**, 2598–2607.

17 Z. Liang, C. Qu, D. Xia, R. Zou and Q. Xu, Atomically Dispersed Metal Sites in MOF-Based Materials for Electrocatalytic and Photocatalytic Energy Conversion, *Angew. Chem., Int. Ed.*, 2018, **57**, 9604–9633.

18 P. Li, Y. Lin, Z. Qi and D. Yan, Efficient photoelectrocatalytic CO_2 reduction to CH_3OH via porous g-C_3N_4 nanosheets modified with cobalt phthalocyanine in ionic liquids, *J. Mater. Chem. A*, 2023, **11**, 21078–21088.

19 Z. Guo, W. Ye, X. Fang, J. Wan, Y. Ye, Y. Dong, D. Cao and D. Yan, Amorphous cobalt–iron hydroxides as high-

efficiency oxygen-evolution catalysts based on a facile electrospinning process, *Inorg. Chem. Front.*, 2019, **6**, 687–693.

20 H. Lyu, T. Hisatomi, Y. Goto, M. Yoshida, T. Higashi, M. Katayama, T. Takata, T. Minegishi, H. Nishiyama, T. Yamada, Y. Sakata, K. Asakura and K. Domen, Domen, An Al-doped SrTiO$_3$ photocatalyst maintaining sunlight-driven overall water splitting activity for over 1000 h of constant illumination, *Chem. Sci.*, 2019, **10**, 3196–3201.

21 X. Fan, T. Wang, H. Xue, B. Gao, S. Zhang, H. Gong, H. Guo, L. Song, W. Xia and J. He, Synthesis of Tungsten Trioxide/Hematite Core–Shell Nanoarrays for Efficient Photoelectrochemical Water Splitting, *ChemElectroChem*, 2019, **6**, 543–551.

22 Q. Xu, H. Jiang, X. Duan, Z. Jiang, Y. Hu, S. W. Boettcher, W. Zhang, S. Guo and C. Li, Fluorination-enabled Reconstruction of NiFe Electrocatalysts for Efficient Water Oxidation, *Nano Lett.*, 2021, **21**, 492–499.

23 K. Bera, A. Karmakar, S. Kumaravel, S. S. Sankar, R. Madhu, H. N. Dhandapani, S. Nagappan and S. Kundu, Vanadium-Doped Nickel Cobalt Layered Double Hydroxide: A High-Performance Oxygen Evolution Reaction Electrocatalyst in Alkaline Medium, *Inorg. Chem.*, 2022, **61**, 4502–4512.

24 S. Chen, H. Liao, X. Xu, R. Wang, Z. Sun and L. Huang, Ga-induced electronic structure engineering of NiFe$_2$O$_4$ nanosheet arrays for stable and efficient oxygen evolution, *Inorg. Chem. Front.*, 2023, **10**, 6320–6328.

25 S. Suleman, Y. Zhang, Y. Qian, J. Zhang, Z. Lin, Ö. Metin, Z. Meng and H. Jiang, Turning on Singlet Oxygen Generation by Outer–Sphere Microenvironment Modulation in Porphyrinic Covalent Organic Frameworks for Photocatalytic Oxidation, *Angew. Chem., Int. Ed.*, 2023, 34450.

26 S. Wang, Z. Ai, X. Niu, W. Yang, R. Kang, Z. Lin, A. Waseem, L. Jiao and H. Jiang, Linker Engineering of Sandwich–Structured Metal–Organic Framework Composites for Optimized Photocatalytic H$_2$ Production, *Adv. Mater.*, 2023, **35**, 202302512.

27 Y. Tang, Z. Zhang, Y. Jin, S. Gao, D. Huang, S. Xu and R. Zou, Kinetic and Thermodynamic Insights into Advanced Energy Storage Mechanisms of Battery-Type Bimetallic Metal–Organic Frameworks, *Chem. Mater.*, 2022, **34**, 10338–10346.

28 Y. Zhang, J. Guo, J. Zhang, X. Qiu, X. Zhang, J. Han, B. Zhang, C. Long, Y. Shi, Z. Yang, W. Zhao and Z. Tang, Metal-organic frameworks enable regio- and stereo-selective functionalization of aldehydes and ketones, *Chem*, 2022, **8**, 1688–1704.

29 T. Qiu, S. Gao, Z. Liang, D. Wang, H. Tabassum, R. Zhong and R. Zou, Pristine Hollow Metal–Organic Frameworks: Design, Synthesis and Application, *Angew. Chem., Int. Ed.*, 2021, **60**, 17314–17336.

30 Z. Lei, X. Jin, J. Li, Y. Liu, J. Liu, S. Jiao and R. Cao, Tuning electrochemical transformation process of zeolitic imidazolate framework for efficient water oxidation activity, *J. Energy Chem.*, 2022, **65**, 505–513.

31 J. Tian, F. Jiang, D. Yuan, L. Zhang, Q. Chen and M. Hong, Electric–Field Assisted In Situ Hydrolysis of Bulk Metal–Organic Frameworks into Ultrathin Metal Oxyhydroxide Nanosheets for Efficient Oxygen Evolution, *Angew. Chem., Int. Ed.*, 2020, **59**, 13101–13108.

32 F. Zhao, B. Wen, W. Niu, Z. Chen, C. Yan, A. Selloni, C. G. Tully, X. Yang and B. E. Koel, Increasing Iridium Oxide Activity for the Oxygen Evolution Reaction with Hafnium Modification, *J. Am. Chem. Soc.*, 2021, **143**, 15616–15623.

33 J. Chen, H. Li, Z. Pei, Q. Huang, Z. Yuan, C. Wang, X. Liao, G. Henkelman, Y. Chen and L. Wei, Catalytic activity atlas of ternary Co–Fe–V metal oxides for the oxygen evolution reaction, *J. Mater. Chem. A*, 2020, **8**, 15951–15961.

34 P. Gao, Y. Zeng, P. Tang, Z. Wang, J. Yang, A. Hu and J. Liu, Understanding the Synergistic Effects and Structural Evolution of Co(OH)$_2$ and Co$_3$O$_4$ toward Boosting Electrochemical Charge Storage, *Adv. Funct. Mater.*, 2022, **32**, 2108644.

35 C. Defilippi, D. V. Shinde, Z. Dang, L. Manna, C. Hardacre, A. J. Greer, C. D'Agostino and C. Giordano, HfN Nanoparticles: An Unexplored Catalyst for the Electrocatalytic Oxygen Evolution Reaction, *Angew. Chem., Int. Ed.*, 2019, **58**, 15464–15470.

36 Q. P. Ngo, T. T. Nguyen, Q. T. T. Le, J. H. Lee and N. H. Kim, Unveiling the Synergistic Effect of Atomic Iridium Modulated Zirconium–Doped Pure Phase Cobalt Phosphide for Robust Anion–Exchange Membrane Water Electrolyzer, *Adv. Energy Mater.*, 2023, **13**, 2301841.

37 Y. Qin, T. Yu, S. Deng, X. Zhou, D. Lin, Q. Zhang, Z. Jin, D. Zhang, Y.-B. He, H. Qiu, L. He, F. Kang, K. Li and T. Zhang, RuO$_2$ electronic structure and lattice strain dual engineering for enhanced acidic oxygen evolution reaction performance, *Nat. Commun.*, 2022, **13**, 3784.

This journal is © the Partner Organisations 2024

Inorg. Chem. Front., 2024, **11**, 5449–5457 | **5457**